



## Buoyant convection resulting from dissolution and permeability growth in vertical limestone fractures

A. Chaudhuri,<sup>1</sup> H. Rajaram,<sup>1</sup> H. Viswanathan,<sup>2</sup> G. Zyvoloski,<sup>2</sup> and P. Stauffer<sup>2</sup>

Received 10 November 2008; accepted 31 December 2008; published 4 February 2009.

[1] Upward flow through vertical fractures in limestone formations under a geothermal gradient favors dissolution and permeability growth. We investigate the transition from conductive and forced convective regimes to instability and buoyant convection as a result of permeability growth. The onset time for instability and roll height at onset depend on the initial aperture and driving pressure. A modified Rayleigh number criterion is proposed, which provides a unified interpretation of the instability across a wide range of initial aperture and driving pressure. Interaction between buoyant convection and aperture alteration leads to narrow upward flow paths supporting dissolution and precipitation in surrounding downward flow regions. **Citation:** Chaudhuri, A., H. Rajaram, H. Viswanathan, G. Zyvoloski, and P. Stauffer (2009), Buoyant convection resulting from dissolution and permeability growth in vertical limestone fractures, *Geophys. Res. Lett.*, 36, L03401, doi:10.1029/2008GL036533.

### 1. Introduction

[2] Feedbacks between fracture alteration and permeability are widely believed to influence permeability evolution and pattern formation in karst systems. For example, localized positive feedback between increased permeability, flux and dissolution rate leads to the formation of distinct channels, a process implicated in the formation of cave systems by meteoric waters [Siemers and Dreybrodt, 1998]. However, cave systems formed under hydrothermal or hypogene conditions exhibit significantly different maze-like patterns whose origin remains to be explained. In a previous study of the early stages of karstification in hydrothermal systems, Andre and Rajaram [2005] investigated fracture growth under conductive and forced-convective heat transfer regimes. They suggested that permeability increase in these regimes could lead to the onset of buoyant convection via the Rayleigh-Benard instability, which would influence subsequent morphological evolution, and potentially explain the origin of maze-like patterns. However, the onset of buoyant convection resulting from dissolution and permeability growth in fractures has not been investigated to date. In this paper, we present numerical simulations to obtain preliminary insights into this complex problem, by considering an idealized system involving a vertical fracture with a uniform initial aperture in a limestone formation. The simulations illustrate a sequence of transitions from an

initial regime of slow upward flow and conductive heat transfer to one of buoyant convection with organized convection rolls.

### 2. Flow and Transport Equations

[3] We consider a fracture within a relatively impermeable host rock. Flow within the rock mass and lateral flow from the rock into the fracture are neglected. The mass balance equation for water flow in the fracture is thus:

$$\frac{\partial(\rho b)}{\partial t} + \nabla \cdot (\rho \mathbf{q}) = 0. \quad (1)$$

In (1)  $b$  is the aperture,  $\rho$  is the density of the water; and  $\mathbf{q}$  is the aperture-integrated water flux through the fracture, given by:

$$\mathbf{q} = -\frac{b^3}{12\mu F_T} (\nabla P - \rho \mathbf{g}), \quad (2)$$

where  $P$  and  $\mu$  are respectively the fluid pressure and dynamic viscosity, and  $\mathbf{g}$  is the gravitational acceleration. The factor  $F_T$  accounts for increased (nonlinear) flow resistance from non-laminar flow, and is related to the local Reynolds number ( $\text{Re} = |\mathbf{q}| \rho / \mu$ ), based on the experimental results of Zimmerman *et al.* [2004] as  $F_T = (1 + 0.00838 \text{ Re})$ . For low  $\text{Re}$ , (2) reduces to the local cubic law. The aperture-integrated energy balance equation for the fracture is

$$\frac{\partial(b\rho C_p T)}{\partial t} + \nabla \cdot (\rho \mathbf{q} h_E - \lambda b \nabla T) = -2\lambda_r \frac{\partial T_r}{\partial y} \Big|_{y=\pm b/2}. \quad (3)$$

In (3)  $T$ ,  $h_E$ ,  $\lambda$  and  $C_p$  are respectively the aperture-averaged fluid temperature in the fracture, enthalpy, thermal conductivity and specific heat of water. The dependence of  $\rho$ ,  $h_E$ , and  $\mu$  on  $T$  and  $P$  are fitted using rational polynomials (G. A. Zyvoloski *et al.*, Finite element heat and mass transfer code (FEHM), available at <http://fehmlanl.gov/>). The right hand side of (3) represents the lateral heat exchange between the fracture and rock, across the two fracture surfaces. Here  $T_r$  and  $\lambda_r$  are respectively the temperature and thermal conductivity of rock. Heat transport in the rock follows the 3-D conduction equation:

$$\frac{\partial T_r}{\partial t} - \kappa_r \nabla^2 T_r = 0, \quad (4)$$

where  $\kappa_r$  is the thermal diffusivity of the rock. The heat transport equations (3) and (4) are coupled via the lateral heat exchange term in (3).

<sup>1</sup>Department of Civil, Environmental and Architectural Engineering, University of Colorado, Boulder, Colorado, USA.

<sup>2</sup>Earth and Environmental Sciences Division, Los Alamos National Laboratory, Los Alamos, New Mexico, USA.

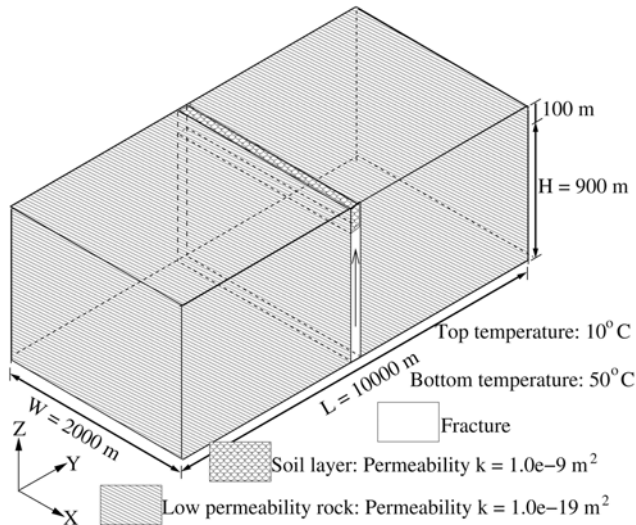


**Figure 1.** Geometry and dimensions of a simple fracture-matrix system. The water flows vertically upward against the geothermal temperature gradient.

[4] The rate of aperture alteration is largely controlled by solubility ( $c_s$ ) gradients resulting from temperature and pressure gradients [Andre and Rajaram, 2005], and thus described by:

$$\frac{\partial b}{\partial t} = \frac{1}{\omega \rho_r} \mathbf{q} \cdot \nabla c_s \quad (5)$$

where  $\rho_r$  is the rock density and  $\omega$  represents the number of moles of soluble mineral per unit mass of rock. On the right hand side of (5), the diffusive/dispersive solute mass flux is neglected, because it is much smaller than the advective flux [Chaudhuri et al., 2008].

[5] For limestone, the dependence of solubility  $c_s$  on temperature and pressure is given by Andre and Rajaram [2005] and Morel [1983]:

$$c_s = (1 + 0.0024(P - P_0))(1.42E-3 - 1.97E-4T - 4E-8T^2) \quad (6)$$

where  $P_0$  is a reference pressure in MPa and  $T$  is in °C. The most important feature of (6) is the retrograde solubility with temperature, which leads to dissolution if fluid cools along a flow path.

### 3. Model Problem and Computational Approach

[6] The schematic computational domain is shown in Figure 1. Along the vertical fracture (1 km deep and 2 km wide), upward water flow is driven by an imposed pressure difference (greater than hydrostatic) between the top and bottom. The bottom temperature is held fixed at 50°C in both the fracture and the rock and a mixed boundary condition is applied at the top which maintains temperature at the upper boundary near the initial condition of 10°C. The initial temperature field follows a geothermal gradient of 0.04°C/m from bottom to top. This variation is prescribed

as a boundary condition at the outer boundaries of the rock mass at all times. A soil layer is defined at the top of the fracture, where permeability is not altered. This avoids potentially unrealistic behavior resulting from imposing a boundary condition at the top of the fracture, where convection cells can lead to inflow or outflow. The coupled flow (1), heat transport (3) and aperture alteration (5) equations were solved numerically by using the software package FEHM (Finite Element Heat and Mass Transfer) (<http://fehm.lanl.gov/>). The capability of FEHM for simulating convection in 3-D porous media was established by Stauffer et al. [1997]. Because FEHM was developed for porous media, simulation of (1)–(5) was accomplished by treating the aperture as an “equivalent porosity” and relating permeability to aperture as implied by (2).

[7] The transient coupling between the buoyancy-influenced fluid flow and heat transport equations controls the variable time-step used in the FEHM simulations. FEHM uses an implicit approach to solve 3-D fluid flow and heat transport equations. The extremely slow rate of aperture alteration justifies an explicit treatment of the coupling between the alteration equation (5) and the flow and transport equations (1, 2, and 3). The computational domain was discretized into a grid of (80 × 25 × 80) volume elements along (x, y, z) directions, with the central (80 × 80) plane of elements representing the fracture. The fracture grid was nonuniform (25 m × 10 m in the upper portion of the fracture, increasing to 25 m × 20 m near the entrance). In the rock, a finer grid (5 cm) was used near the fracture-rock interface.

### 4. Results and Discussion

[8] Based on numerical simulations across a wide range of system parameters, we identified 4 distinct stages in the evolution of the fluid flow and thermal regime. In Stage 1, heat transfer is conduction dominated and the constant temperature, pressure (and solubility) gradients result in relatively uniform dissolution and aperture growth. Eventually, the permeability and fluid flux increase, forced-convective heat transfer effects become significant, and the temperature gradient becomes flat near the entrance (Stage 2, see Figure 2b). As a result, aperture growth slows down in the lower portion of the fracture, while it remains significant in the upper portion, leading to a nonuniform aperture profile (see Figure 2a). Up to this point, the behavior is similar to that previously identified by Andre and Rajaram [2005]. Stage 3 corresponds to the onset of buoyant convection in the upper portion of the fracture, where both the permeability and density gradient are large, typified by undulation of the temperature field (Figure 2b) and roll patterns in the flow field (Figure 2c). Once the buoyant-convection regime of Stage 3 is established, the aperture grows where the water flows up (cooling), and reduces where the water flows down (warming). This leads to the formation of narrow dissolution channels supporting upward flow, as seen in Figures 2d and 2f. As shown in Figures 2e and 2f, the convection rolls gradually extend to the middle of the fracture plane, some of them combine together and finally a few large rolls persist (Stage 4). The total upward flux out of the fracture increases significantly during the conduction and forced convection regimes, but

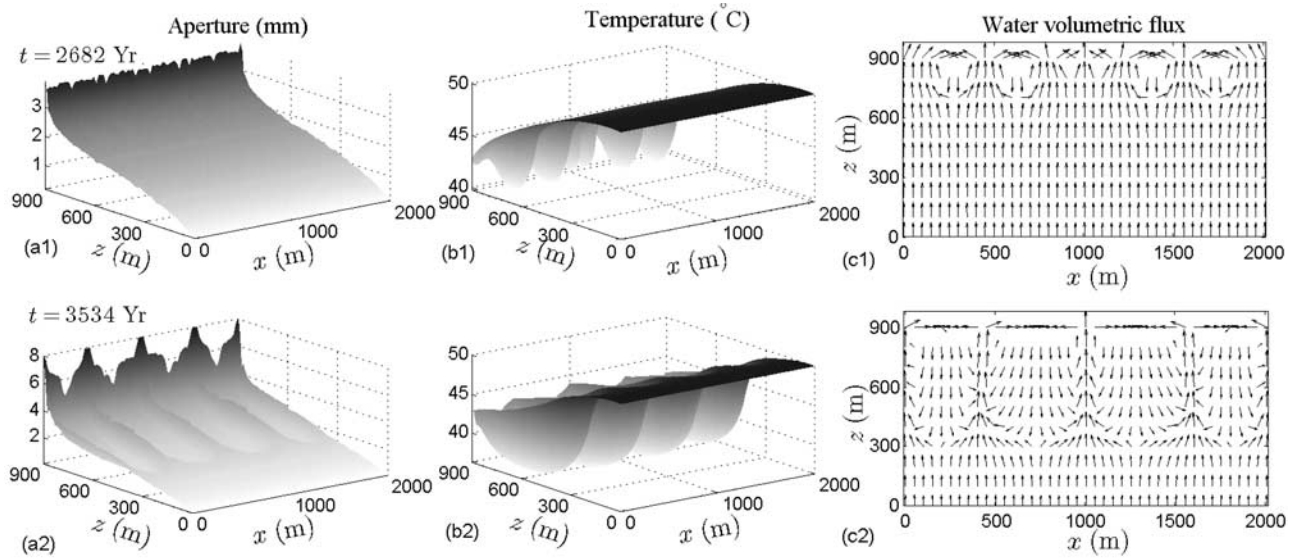


**Figure 2.** Aperture, corresponding temperature and flux fields (magnitudes are in log scale) at two different times for  $b_0 = 0.3$  mm and  $\Delta P = 10.0$  MPa: (a–c) just after the onset of buoyant convection and (d–f) final configuration with narrow upward flow channels.

does not vary significantly with time in the buoyant convection regime.

[9] The main factor responsible for the onset of buoyant convection (transition from Stage 2 to 3) is aperture growth. The aperture growth rate depends on the magnitude of the upward flux and solubility gradient (see 5). The magnitude of the initial upward flux depends on initial aperture ( $b_0$ ) and pressure difference ( $\Delta P$ ). Thus, for a given  $c_s(T, P)$  function, we consider  $b_0$  and  $\Delta P$  as the key system parameters influencing the Stage 2–3 transition, characterized by the onset time for buoyant convection ( $t_b$ ) and the height of the convection rolls ( $H_{\text{roll}}$ ) at onset. Figures 3a and 3b

show the variation of  $t_b$  and  $H_{\text{roll}}$  (estimated by visual examination of the simulated flow fields) with  $b_0$  and  $\Delta P$ . At low values of  $\Delta P$ ,  $t_b$  is quite sensitive to  $b_0$ ; for small  $b_0$ , the initial aperture growth rate is also small, Stage 1 is longer, and thus  $t_b$  is larger. At small values of  $b_0$ ,  $t_b$  decreases with  $\Delta P$  because an increase in  $\Delta P$  leads to an increased flux (hence growth rate), decreasing the duration of Stage 1. For large values of  $b_0$ , Stage 1 is relatively short-lived, but Stage 2 is long and  $t_b$  increases as  $\Delta P$  increases because stronger forced convection inhibits buoyant convection. For large values of  $\Delta P$ ,  $t_b$  is relatively insensitive to  $b_0$ . The behavior at high  $b_0$  involves some very subtle

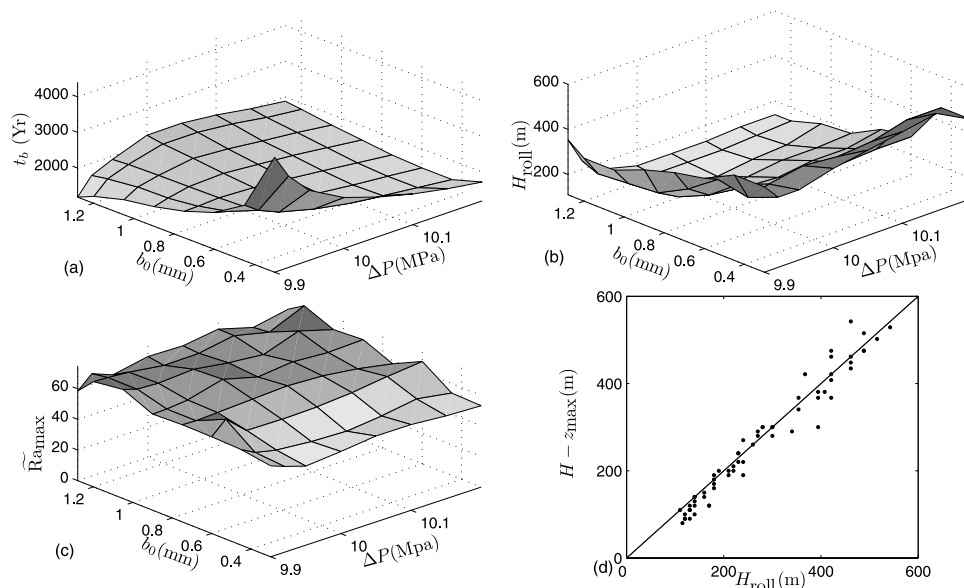


**Figure 3.** Characteristics of the onset of the buoyant convection for a range of ( $b_0$ ) and ( $\Delta P$ ): (a) time required for onset  $t_b$ , (b) height of convection rolls (visually determined from flux field),  $H_{\text{roll}}$ , (c) maximum Rayleigh number,  $\tilde{Ra}_{\text{max}}$  and (d) comparison of  $H_{\text{roll}}$  with  $H - z_{\text{max}}$ .

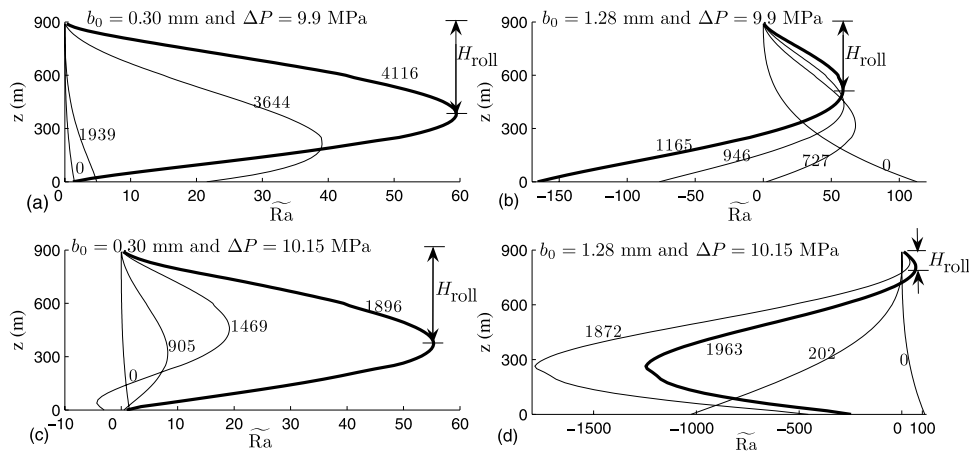


**Figure 4.** Time evolution of the modified Rayleigh number  $\widetilde{Ra}(z, t)$  for different cases. The labels on the curves correspond to time (years). The thick curves correspond to the onset of buoyant convection.

effects: due to the large fluid flux, the forced-convective regime persists for a long time; in the absence of a significant temperature gradient, the pressure dependence of solubility plays an important role, causing slow precipitation due to a negative pressure gradient. Aperture reduction by precipitation causes a reduced flux, and the strength of the forced-convective regime reduces slowly, facilitating transition to a buoyant-convective regime. It should be noted that if the pressure dependence of calcite solubility is not represented, the forced-convective regime will persist forever at high  $b_0$ , with no transition to buoyant convection. The roll height at the onset of buoyant convection is small ( $\approx 110$  m) at high  $b_0$  and  $\Delta P$ , because of the inhibitory influence of forced convection; and increases as  $b_0$  and  $\Delta P$  decrease. The late-time (Stage 4) convection roll pattern involves 4 to 8 rolls for the configuration of the fracture plane considered. No specific trend was observed in the number of rolls or the roll height ( $\approx 600$  m) as a function of  $b_0$  and  $\Delta P$  in stage 4.

[10] To gain more insight into the onset of buoyant convection (Stage 2–3 transition), we draw upon previous studies of the instability of stagnant fluid in a vertical fracture exchanging heat with a rock mass in a geothermal gradient (but without reactive alteration). *Murphy* [1979] concluded that the instability is largely controlled by transient heat exchange with the rock mass, which has a stabilizing influence that decreases with time. His analysis suggests that early-time “spontaneous” instability can only occur if the Rayleigh number  $Ra >$  approximately  $10(H/b)^2$  ( $H$  is the system height and  $b$  is the constant fracture aperture), which is practically impossible in the typical range of fracture apertures. He also showed that a “delayed” instability can occur if there are sustained perturbations to the temperature field, due to the diminishing influence of heat exchange with the rock. Although *Murphy* [1979] suggested that the critical  $Ra$  for delayed instability decreases as  $1/\sqrt{t}$ , subsequent numerical simulations by *Tournier et al.* [2000] with finite rock thickness show that it is a constant value, proportional to  $(H/b)$  (i.e.  $Ra(b/H)$  is constant at onset of instability). These results need to be modified for our situation, which is complicated by aperture growth, vertical ( $z$ ) variations in aperture,

permeability and density gradient, and alteration of temperature gradients by forced convection. We therefore define the following modified Rayleigh number  $Ra(z, t)$ :

$$Ra(z, t) = \frac{K_{\text{eff}}(z, t) \Delta \rho(z, t) (H - z)}{\rho_0 \kappa} \quad (7)$$

where  $\rho_0$  is the reference density of the water entering from the bottom,  $K_{\text{eff}}(z, t)$  and  $\Delta \rho(z, t)$  are respectively the effective hydraulic conductivity (computed as the harmonic average) and the density difference that control instability across the height  $H - z$ :

$$K_{\text{eff}}(z, t) = \left( \frac{1}{H - z} \int_z^H \left( \frac{b^2(z', t) g}{12 \nu(z', t) F_T(z', t)} \right)^{-1} dz' \right)^{-1},$$

$$\Delta \rho(z, t) = \rho(H, t) - \rho(z, t) \quad (8)$$

During the conductive and forced-convective regimes preceding instability, all the properties are uniform along the  $x$  direction, thus the  $x$  dependence in (7) and (8) is dropped. While  $H - z$  reduces with  $z$ , both  $K_{\text{eff}}(z, t)$  and  $\Delta \rho(z, t)$  increase with  $z$  in the forced-convective regime. Consequently  $Ra(z, t)$  will vary non-monotonically with  $z$ . We use  $z_{\text{max}}$  to denote the vertical location of the maximum value of  $Ra(z, t)$ . Motivated by *Tournier et al.* [2000], and noting that the most favorable condition for instability is between  $z_{\text{max}}$  and  $H$ , we multiply  $Ra(z, t)$  with a quantity analogous to their  $(b/H)$  to analyze the instability:  $\widetilde{Ra}(z, t) = Ra(z, t) (\bar{b}(z_{\text{max}}, t) / (H - z_{\text{max}}))$  where  $\bar{b}(z_{\text{max}}, t)$  is the average aperture between  $z_{\text{max}}$  and  $H$ . The effective height of the rolls in defining  $\widetilde{Ra}(z, t)$  is taken to be  $H - z_{\text{max}}$ . The time evolution of  $\widetilde{Ra}(z, t)$  during Stage 2 is shown in Figures 4a to 4d for 4 different pairs of  $b_0$  and  $\Delta P$ . For smaller  $b_0$  (Figures 4a and 4c), the maximum Rayleigh number,  $\widetilde{Ra}_{\text{max}}$  increases with time, and the instability occurs when  $(\widetilde{Ra}_{\text{max}})$  exceeds a critical value  $\widetilde{Ra}_{\text{crit}}$ . For larger  $b_0$ , (Figures 4b and 4d) the initial  $\widetilde{Ra}(z, 0)$  has a maximum value at  $z = 0$ , which is larger than the maximum value at later times, yet no instability occurs because the spontaneous instability criterion is not satisfied. With time, there is a significant region in the lower portion of the fracture where  $\widetilde{Ra}(z, t)$  is

negative, indicating stable density distributions. However, in the upper portion of the fracture,  $Ra(z, t)$  remains positive and develops a profile, with a maximum that increases with time. The delayed instability occurs when the positive maximum of  $Ra(z, t)$  exceeds  $\widetilde{Ra}_{crit}$ . Figure 3c shows the value of  $\widetilde{Ra}_{max}$  at the onset of instability, across different  $b_0$  and  $\Delta P$ , which confirms that  $\widetilde{Ra}_{max}$  at the time of onset is almost constant for all cases considered, and  $\widetilde{Ra}_{crit}$  is in the range of 50–70. The minor variations of  $\widetilde{Ra}_{crit}$  across the different cases reflect the secondary influence of the detailed  $z$ -variation of aperture and density gradient. Finally Figure 3d shows that  $H_{roll}$  estimated from visual analysis of the flux fields at the onset of convection corresponds very well with  $H - z_{max}$  for the entire range of  $b_0$  and  $\Delta P$  considered.

## 5. Conclusions

[11] The key conclusions of the paper are that (i) across a wide range of initial aperture ( $b_0$ ) and driving pressure difference ( $\Delta P$ ), growth of vertical fractures by dissolution in limestone formations indeed leads to the onset of buoyant convection; (ii) the time required for the onset of buoyant convection and the roll height at onset vary with  $b_0$  and  $\Delta P$ , and is of the order of a few 1000's of years in the parameter range considered; (iii) a modified Rayleigh number  $\widetilde{Ra}_{max}$  provides a unified interpretation of the onset of instability, attaining a relatively constant critical value  $\widetilde{Ra}_{crit}$  between 50 and 70; (iv) after the onset of buoyant convection, feedback between fracture alteration and the flow field continues, with precipitation in downward flow zones and dissolution in upward flow zones, leading to the formation of distinct narrow upward flow channels. Due to computational limitations and the complexity of the problem, we considered the idealized case of a single fracture in this paper. In future work, we will focus on the behavior in variable-aperture fractures exhibiting preferential flow and

fracture networks, also including other complexities such as dissolution/precipitation kinetics. Our conjecture is that hypogene cave systems can develop in the upflow zones following onset of buoyant convection, and their morphology may be further influenced by the fracture network.

[12] **Acknowledgments.** We gratefully acknowledge financial support from the Institute for Geophysics and Planetary Physics at Los Alamos National Laboratory (grant IGPP Geo 1714).

## References

- Andre, B. J., and H. Rajaram (2005), Dissolution of limestone fractures by cooling waters: Early development of hypogene karst systems, *Water Resour. Res.*, *41*, W01015, doi:10.1029/2004WR003331.
- Chaudhuri, A., H. Rajaram, and H. Viswanathan (2008), Alteration of fractures by precipitation and dissolution in gradient reaction environments: Computational results and stochastic analysis, *Water Resour. Res.*, *44*, W10410, doi:10.1029/2008WR006982.
- Morel, F. M. M. (1983), *Principles and Applications of Aquatic Chemistry*, John Wiley, New York.
- Murphy, H. D. (1979), Convective instability in vertical fractures and faults, *J. Geophys. Res.*, *84*(11), 6121–6130.
- Siemers, J., and W. Dreybrodt (1998), Early development of karst aquifers on percolation networks of fractures in limestone, *Water Resour. Res.*, *34*(3), 409–419.
- Stauffer, P. H., L. H. Auer, and N. D. Rosenberg (1997), Compressible gas in porous media: A finite amplitude analysis of natural convection, *Int. J. Heat Mass Transfer*, *40*(7), 1585–1589.
- Tournier, C., P. Genthon, and M. Rabinowicz (2000), The onset of natural convection in vertical fault planes: Consequences for the thermal regime in crystalline basements and for heat recovery experiments, *Geophys. J. Int.*, *140*, 500–508.
- Zimmerman, R. W., A. Al-Yaarubi, C. C. Pain, and C. A. Grattoni (2004), Nonlinear regimes of fluid flow in rock fractures, *Int. J. Rock Mech. Min. Sci.*, *41*(3), 384.

A. Chaudhuri and H. Rajaram, Department of Civil, Environmental and Architectural Engineering, University of Colorado, Boulder, CO 80309, USA. (hari@colorado.edu)

P. Stauffer, H. Viswanathan, and G. Zyvoloski, Earth and Environmental Sciences Division, Los Alamos National Laboratory, Los Alamos, NM 87545, USA.